

November 25, 2002

Tensile Creep of Polycrystalline Near-Stoichiometric NiAl

S. V. Raj

NASA Lewis Research Center, MS 24-1
21000 Brookpark Road, Cleveland, OH 44135

ABSTRACT

Long term tensile creep studies were conducted on binary NiAl in the temperature range 700-1200 K with the objectives of characterizing and understanding the creep mechanisms. Inverse and normal primary creep curves were observed depending on stress and temperature. It was concluded that the creep of NiAl is limited by dislocation mobility. The stress exponent for creep, n , increased from 5.5 at 1200 K to 13.9 at 700 K. The true activation energy for creep, Q_c , was constant and equal to about 400 kJ mol⁻¹ between 20 and 50 MPa but decreased to a constant value of 250 kJ mol⁻¹ between 50 and 110 MPa. The activation energy was observed to be stress dependent above 110 MPa. The tensile creep results reported in this investigation were compared with compression creep data reported in the literature. A detailed discussion of the probable dislocation creep mechanisms governing compressive and tensile creep of NiAl is presented. It is concluded that the non-conservative motion of jogs on screw dislocations influenced the nature of the primary creep curves, where the climb of these jogs involves either the next nearest neighbor or the six-jump cycle vacancy diffusion mechanism. The probable nature of the atom-vacancy exchange that occur within the core of an edge dislocation undergoing climb in NiAl are schematically examined.

This report is a preprint of an article submitted to a journal for publication. Because of changes that may be made before formal publication, this reprint is made available with the understanding that it will not be cited or reproduced without the permission of the author.

I. INTRODUCTION

Over the last several decades, a considerable amount of research has been conducted on developing NiAl-based alloys for use in gas-turbine aircraft engines. An attractive combination of oxidation, physical and thermal properties make NiAl¹ a potentially useful material for fabricating turbine blades to withstand temperatures above 1200 K. However, the inherent low temperature brittleness of the material combined with its poor elevated temperature creep properties has prevented its development as ~~4~~ rotating and stationary hardware in aircraft engines. ✓

A fundamental understanding of the creep mechanisms dominant in NiAl is important in order to develop methods to improve its high temperature creep strength. A review of the literature reveals that most of the investigations conducted on polycrystalline binary NiAl at elevated temperatures were in compression both under constant strain rate [1,2,3,4,5] and under constant load or stress [6,7,8,9,10,11,12,13,14,15,16,17] conditions. Except for one reference source [18], virtually no tensile creep data exist on polycrystalline NiAl. Even in this case, the published data were scant and no details were provided on composition, processing conditions, grain size and activation energy for creep. Although some tensile creep data have been reported on near-stoichiometric NiAl single crystals [19,20], other single crystal data have been determined in either constant strain rate [21] or constant load [22,23] compression tests. The importance of obtaining tensile creep data on polycrystalline NiAl is not only useful for comparing with the compression creep data to ensure that its creep properties are independent of the macroscopic state of stress but also for establishing a database for alloy and structural design purposes.

The present study was motivated with the intention of fulfilling three objectives: First, to generate long term tensile creep data on polycrystalline NiAl over a wide range of stresses and temperatures; second, to characterize and evaluate the creep mechanisms dominant under these test conditions; and third, to compare the tensile and compression creep data to identify the similarities and differences between the two sets of results. The present paper expounds on some of the preliminary results presented in earlier publications [24,25].

II. EXPERIMENTAL MATERIALS AND PROCEDURES

The materials used in this study were obtained from two heats of induction melted NiAl, where a high purity charge of Al and Ni pellets were melted in an alumina crucible to produce two nominally stoichiometric NiAl ingots (~ 1000 g). The molten alloy was cast into split copper molds about 25.4 mm in diameter and 150 mm long and allowed to cool to room temperature. After cropping their hot-tops, the two ingots were ~~cropped~~ vacuum-sealed in mild steel cans and extruded at 1400 K using ratios of 16:1 (L 3175) and 20:1 (L 3176). The compositions and grain sizes of the two extruded rods of material are given in Table 1, where it is evident that the choice of these two extrusion ratios did not significantly alter the final grain sizes of the extruded rods². The major elements were determined by inductively-coupled plasma (ICP) analysis, while carbon was analyzed by the combustion extraction method. Nitrogen and oxygen were determined by the inert gas fusion technique. Optical microscopy observations and quantitative measurements of the longitudinal and transverse grain sizes, d , of the extruded rods revealed that the grains were

¹ All compositions are given in atomic percent in the paper unless otherwise specified.

² Although batch L 3176 had a significantly larger amount of carbon than batch L 3175, its effect could not be separated from normal experimental scatter in the creep data.

equiaxed and fully recrystallized (Fig. 1). Grain size measurements were conducted by linear intercept analysis. The mean values of the grain size are reported in Table 1, where the errors in measurement represent the 95% confidence limits.

Smooth button-head tensile specimens having gage lengths of 30.5 mm and gage diameters of 3.0 mm were centerless ground from the extruded rods (Fig. 2(a)). Specimens with ridges for attaching the creep extensometer at the gage length were also used in a few tests to determine the primary creep strain accurately (Figs. 2(b) & (c)). The machined surfaces were removed by electropolishing in a 10% perchloric acid-90% methanol bath prior to testing. Constant load tensile creep tests were conducted in air using lever arm machines at absolute temperatures, T , between 700 and 1200 K under initial applied stresses, σ_e , varying between 10 and 170 MPa. Most of the specimens tested in the temperature range 900-1200 K were machined from extrusion L 3176, whereas all the specimens tested at 700 and 800 K were obtained from L 3175. Three thermocouples were attached along the gage length of the specimen and the accuracy of temperature control and the temperature gradient along the gage length were ± 1 K. The specimen load train was allowed to stabilize at temperature for at least 1 h before loading. The elongation of the specimen corresponding to the design shown in Fig. 2(a) was measured by attaching an extensometer to the top and bottom couplings in most of the tests, where the displacement of the extensometer heads was measured either by a linear variable displacement transformer (LVDT) or a super linear variable capacitance (SLVC) transducer. However, the specimen designs shown in Fig. 2 (b) & (c) allowed the extensometer to be attached to the ridges, and therefore, permitted the specimen elongation to be measured with greater precision. The elongation and temperature data were continuously monitored by a computerized data acquisition

system. Most of the specimens were tested until rupture except in the case of a few long-term tests, which were terminated. In order to assess the nature of the transients after a stress change, a specimen was crept at 900 K, where the engineering stress was changed between 40 and 50 MPa until rupture. The tested specimens were longitudinally sectioned and polished parallel to the stress axis for viewing under an optical microscope. The final grain sizes, d_f , were determined both in the undeformed shoulder and in the deformed longitudinal gage sections in a few specimens away from the fracture zone in order to evaluate the extent of grain growth during the test.

III. RESULTS

Deformation behavior

The shape of the creep curves

Figures 3(a-c) show the typical tensile creep curves for NiAl, plotted as the true creep strain, ϵ , against time, t , in the temperature range 700 to 1200 K under initial applied stresses varying between 10 and 170 MPa. The corresponding plots of the true creep rate, $\dot{\epsilon}$, against ϵ are shown in Figs 4 (a-c), where the measured creep rates typically vary between 10^{-10} and 10^{-4} s^{-1} . Since the data were obtained under constant load conditions, the creep rate increases gradually with increasing strain under quasi-steady-state conditions due to the fact that the specimen cross-sectional area continues to decrease and the true stress continues to increase during deformation (Figs 4(a-c)). It is important to note that the minimum creep rates shown in Fig. 4 do not always represent steady-state values. Unlike pure metals, where steady-state deformation can occur typically after $\epsilon > 10\%$, polycrystalline NiAl exhibits quasi-steady-state behavior when $\epsilon > 2\%$.

At 700 K, the creep rate decreases soon after loading, where this initial decrease is steep at 100 and 120 MPa but relatively gradual at higher stresses (Fig. 4(a)). Two distinct shapes are noticeable in the primary transients depending on the magnitudes of the stress. Inverse primary creep occurs at and below 135 MPa, whereas normal primary creep transient is observed at higher stresses (Figs. 3(a) & 4(a)). Similar creep curves are also observed at 900 K, where the transition from inverse to normal primary creep occurs above 70 MPa. At 1200 K, except for the specimen deformed at 13 MPa, which exhibits an apparent inverse transient behavior, only normal primary creep behavior is observed. Inverse and normal primary creep transients were also observed in both as-cast [6,14] and powder-metallurgy extruded NiAl specimens tested in compression [11,13]. In contrast to the inverse and normal primary creep behavior shown in Figs 3 & 4, the specimen deformed at 1200 K under an initial stress of 10 MPa underwent several stages of normal primary transient behavior over 9100 h (Fig. 5). Similar primary curves have been observed during creep of Pb and these have been attributed to dynamic recrystallization [26]. However, long term tests conducted at other stresses and temperatures, while revealing inverse or normal primary creep transients, did not show similar multiple normal primary creep transient behavior (Fig. 5). The final grain sizes of several specimens from these long term experiments are shown in Table 2 along with the testing conditions, where it is clear that there was considerable grain growth during the duration of these tests. An analysis of the data revealed that the final grain size was given by the relation

$$(d_f/d) = 17.2 t_r^{0.14} \sigma_e^{0.94} \exp(-46.0/RT) \quad (R_d^2 = 0.945) \quad (1)$$

where t_r is either the rupture life or the time at which the test was stopped, R is the universal gas constant, R_d^2 is the coefficient of determination and the activation energy for grain growth is in units of kJ mol^{-1} .

Figures 6(a-c) show the shape of the creep transients at 900 K after a series of engineering stress changes varying between 40 and 50 MPa. The true creep strain is plotted against time in Fig. 6(a), while the variation of the true creep rate with either true strain or time is shown in Figs. 6(b) & (c), respectively. The magnitudes of the true stresses, σ , before and after each stress change are also shown in Figs. 6(b) & (c). Prior to the first stress change from $\sigma_e = 40$ to 50 MPa, the magnitude of the true creep strain was extremely small at 40 MPa even after 300 h and the shape of the primary creep curve could not be discerned (Fig. 6(a)& (c)). Although the creep rates could not be determined with any degree of precision, it was estimated that they would be between 10^{-10} and 10^{-9} s^{-1} . On increasing the stress to 50 MPa, the creep rate initially increases from about $7.8 \times 10^{-9} \text{ s}^{-1}$ at $\sigma = 40.2 \text{ MPa}$ to about $4.5 \times 10^{-8} \text{ s}^{-1}$ for $\sigma = 50.2 \text{ MPa}$ exhibiting a trend characteristic of class A behavior in many solid solution alloys (Figs. 6(a-c)). As demonstrated in Fig. 4(b), inverse primary creep occurs at a similar value of stress and the creep transient observed in Figs. 6(a-c) is consistent with the expected trend. On decreasing the stress from 50 to 40 MPa, the transient creep behavior is now similar to the class M response reported for pure metals [27], where the creep rate first decreases to a minimum value for about 14 h after the load drop (Fig. 6(c)) before increasing with increasing strain (Fig. 6(b & c)). In this case, the true stress following the stress drop was 49.2 MPa. This observation is contrary to the class A transient response that would be normally expected under conditions when inverse primary creep is observed (Fig. 4(b)). A third stress change from 40 to 50 MPa confirms the occurrence of class M or pure metal behavior, where the creep rate continues to decrease from an initially high value

after the stress increase as deformation progresses. In this case, the creep rate is higher than the extrapolated creep rate observed after the first stress increase by over a factor of five due to an increase in the magnitude of the true stress from a value of 64.6 MPa soon after the stress increase to a final value of 75.7 MPa. Noting that the true stress soon after the stress increase is 64.6 MPa, a class A transient behavior is expected to occur at this value of stress based on the fact that inverse primary creep is observed between 60 and 70 MPa in Fig. 4(b). However, this behavior is not observed in Fig. 6, where instead a class M transient is observed.

Stress dependence of the secondary creep rate

Since the creep rates increased gradually with increasing strain in the quasi-steady-state region in the $\dot{\epsilon}$ - ϵ plots, it was not possible to determine a unique steady-state creep rate from these plots. Instead, the secondary creep rates were determined by linearly regressing the ϵ - t data over the quasi-steady-state region. Figure 7 shows the double logarithmic plots of $\dot{\epsilon}$ against σ between 700 and 1200 K under stresses varying between 10 and 170 MPa, where the secondary creep rates vary between 10^{-10} and 10^{-4} s^{-1} . In this case, σ is the average value of the true stress determined over the same region of the ϵ - t plot which yielded the secondary creep rate. The single datum point shown at 1200 K under an initial stress of 10 MPa, which underwent dynamic recrystallization (Fig. 5), was not considered in the regression analysis since it lies close to the datum point at 1100 K under an identical initial stress. The regression lines through the data are also shown assuming the power-law relation:

$$\dot{\epsilon} = A_1 \sigma^n \quad (2)$$

where A_1 is a microstructure and temperature dependent constant and n is the creep stress exponent. The magnitudes of A_1 , n and R_d^2 , are tabulated in Table 3, where it is seen that n decreases from 13.9 at 700 K to 4.9 at 1200 K. The data at 1000 K exhibit a break in the $\dot{\epsilon}$ - σ plot, where n is 5.1 below 35 MPa and 12.3 above this value of stress.

Temperature dependence of the secondary creep rate

Figure 8 shows Arrhenius plots of $\dot{\epsilon}T/E$ against $1/T$, where E is the Young's modulus, for different σ varying between 15 and 150 MPa corresponding approximately to normalized stresses, σ/E , varying between 8.9×10^{-5} and 7.6×10^{-4} . Since $\dot{\epsilon}$ for the specimen deformed at 1200 K under an applied stress of 10 MPa is closer to the 1100 K data in Fig. 7, it was not possible to accurately determine Q_c at stresses lower than 15 MPa. The creep rates were normalized by the factor (T/E) in accordance with the semi-empirical universal power-law creep equation proposed by Mukherjee *et al.* [28], where the temperature dependence of E was determined from the equation

$$E = 2.37 \times 10^5 - 51T \text{ (MPa)} \quad (3)$$

obtained from a linear regression fit to experimental data [29]. The data shown in Fig. 8 were primarily determined from multiple specimen tests at identical stresses. However, in some instances, additional temperatures were included in order to improve the statistical estimate of Q_c , where these data were estimated from the regression constants given in Table 3.

The magnitudes of the true activation energies for creep, Q_c , determined from the slopes of the Arrhenius plots shown in Fig. 8 are given in Table 4 at different values of the applied stress and plotted in Fig. 9. The broken horizontal line represents the activation energy for lattice

self-diffusion of Ni, Q_{Ni}^* , in near-stoichiometric NiAl based on tracer diffusion measurements, which have been determined to be about 305 [30] and 290 kJ mol⁻¹ [31]. Four deformation regimes are observed in Fig. 9, where the boundaries between regimes I and II, and II and III, are arbitrarily marked as the stresses at which $Q_c = 290$ kJ mol⁻¹. In regime I, the activation energy is less than 290 kJ mol⁻¹, presumably tending towards a constant value of 100 kJ mol⁻¹ as reported earlier for powder-metallurgy (PM) extruded NiAl tested in compression creep [11,13]. In this case, a corresponding value of $n \sim 2$ was observed and it was concluded that a grain boundary sliding mechanism was dominant in this regime. The activation energy for creep is approximately independent of stress in regime II with an average value of about 400 kJ mol⁻¹ determined from the two datum points for which $Q_c > 385$ kJ mol⁻¹. This value is much higher than that reported for PM-extruded NiAl tested in constant load compression for which $Q_c \approx 290$ kJ mol⁻¹ [13] and for cast and extruded NiAl, where $Q_c \approx 300$ kJ mol⁻¹ [14]. It is also higher than Q_{Ni}^* as well as the values of the activation energies for interdiffusion in stoichiometric NiAl, which have been measured to be about 195 kJ mol⁻¹ [32] and about 355 kJ mol⁻¹ [33]. For comparison, an activation energy of about 360 kJ mol⁻¹ was determined from interdiffusion measurements on Ni-48(at.%)Al [34]. The activation energy for creep in regime III decreases to a constant value of about 250 kJ mol⁻¹, which is about 0.86 Q_{Ni}^* and about 0.63 Q_c observed in regime II.

The activation energy for creep decreases linearly with increasing stress in regime IV. A similar decrease in activation energy with increasing stress [1,7] or normalized stress [13] was reported in other investigations on the compressive creep of polycrystalline NiAl. A linear regression analysis through three datum points suggested that

$$Q_c = 442.2 - 1.75 \sigma \quad (R_d^2 = 0.952) \quad (4)$$

where Q_c and σ are in kJ mol^{-1} and MPa, respectively.

When the stress dependence of the entropy term in the rate equation is negligible, the apparent activation volume for creep, V^* , can be estimated from eqn. (4) using [35,36],

$$V^* = -2 (\partial Q_c / \partial \sigma)_T \quad (5)$$

assuming that $\sigma = 2\tau$, where τ is the shear stress. Thus, $V^* \approx 245 b^3$, where b is the Burgers vector ($b = 0.2876 \text{ nm}$). This value is within the same order of magnitude as other values of 75-350 b^3 reported in the literature [1,13]. Similarly, Xu and Arsenault [5] reported values of V^* varying between 50 and 250 b^3 for binary NiAl determined from constant engineering strain rate tests.

Alternatively, instead of the linear fit to the three data points described by eqn. (4), other regression fits assuming a $\sigma^{1/2}$ and σ^{-1} dependence gave the following regression equations:

$$Q_c = 655.1 - 38.7 \sigma^{1/2} \quad (R_d^2 = 0.939) \quad (6(a))$$

$$Q_c = 14.2 + 25,511.7 \sigma^{-1} \quad (R_d^2 = 0.891) \quad (6(b))$$

where once again Q_c and σ are in kJ mol^{-1} and MPa, respectively. It is important to note that some of the models formulated to describe the cross-slip of screw components of dislocations predict the stress dependence given by eqns. (4), 6(a) and (b) at low stresses [37], while eqn.(4) also represents the general formulation for other thermally activated mechanisms [35,36]. The corresponding values of V^* for equations 6(a) & (b) are $38.7/\sigma^{1/2}$ and $51,023.4/\sigma^{-2}$ in the appropriate units of volume. The difference in the magnitudes of R_d^2 between eqns. (4) & (5) is not significant enough to choose between the two types of stress dependencies given the scatter in the data.

The values of n and Q_c were also determined by multiple regression analysis of the data shown in Fig. 7. In this case, creep data obtained below 50 MPa were separately regressed from those determined at and above 50 MPa, where this transition stress was chosen based on the point of transition in the low and high stress exponents observed at 1000 K (Fig. 7). Referring to Fig. 9, the data lying below 50 MPa correspond to regimes I and II, while most of the data lying above this value of stress lie within regimes III and IV. Thus, the regressed results are expected to be influenced to some extent by these transitions. The regressed equations are given below:

$$\dot{\epsilon} = 5.3 \times 10^4 \sigma^{5.9} \exp(-410.2 \pm 14.5/RT) \quad (R^2_d = 0.946) \quad (\sigma < 50 \text{ MPa}) \quad (7)(a)$$

$$\dot{\epsilon} = 7.6 \times 10^{-12} \sigma^{10.1} \exp(-230.9 \pm 8.6/RT) \quad (R^2_d = 0.908) \quad (\sigma \geq 50 \text{ MPa}) \quad (7)(b)$$

where $\dot{\epsilon}$, σ and Q_c are in s^{-1} , MPa and $kJ \text{ mol}^{-1}$, respectively. Clearly, these values of Q_c are generally consistent with those determined from Fig. 8 and shown in Fig. 9.

IV DISCUSSION

Primary tensile creep behavior

An examination of the shape of the tensile creep curves between 700 and 1200 K generated under initial stresses between 10 and 170 MPa reveals three types of primary creep behavior after the initial steep drop in the creep rate soon after loading (Figs. 3-5). Normal primary creep is observed at high stresses and high temperatures, where the creep rate continues to decrease towards a quasi-steady-state value with increasing strain. At low stresses and low

temperatures, inverse primary creep transients are observed as deformation continues beyond the minimum creep rate, and the creep rate increases with increasing creep strain towards a quasi-steady-state behavior. A third type of creep behavior involving a series of multiple normal primary creep transients was also observed at 1200 K under an initial applied stress of 10 MPa (Fig. 5). This type of primary creep behavior is normally attributed to dynamic recrystallization in the literature [26].

A consistent picture emerges when the above observations are mapped out in σ_e -T space as shown in Fig. 10, where open, solid and half-solid circles represent inverse (I), normal (N) and multiple (M) normal primary transients, respectively³. Figure 10 clearly reveals that the observed primary transient behavior is acutely dependent on the magnitudes of stress and temperature. Inverse primary creep is observed at stresses and temperatures corresponding to the shaded region. Normal primary creep occurs at other stresses and temperatures above and below this area. The position of the lower boundary of the shaded region is ill defined due to an absence of low stress data below 1100 K and this is shown as a broken curve. For example, under an initial stress of 40 MPa, there is a transition from inverse to normal primary creep above 1050 K in the temperature. Similarly, at 1100 K, the present observations suggest a transition from normal to inverse and back to normal primary creep transient with increasing stress. Likewise, both Cu-30%Zn [38] as well as Fe-1.5 (at.%)Mo [39] also exhibit similar trends in the nature of the primary creep transients.

³ It should be noted that although the M-type curves may be due to microstructural instability, there is no other distinction between them and the single normal primary N-type curves. Hence, these two curves are treated as a single entity in this discussion.

The occurrence of inverse primary creep is due to a low initial density of mobile dislocations at the start of the creep test. This situation is likely to occur when the density of active dislocation sources is low or the mobility of dislocations is impeded in some way by such factors as high Peierls forces [40,41,42], jogs on screw dislocations [43,44,45], solute atoms [40], short range ordering [40,46], long range ordering [46] or the nucleation of sessile dislocations resulting from the decomposition of a perfect dislocation core [47]. Many solid solution alloys, such as Al-5(at.%) Mg, generally show transitions from $n \approx 5$ to $n \approx 3$ and back to $n \approx 5$ with increasing stress and decreasing temperature, where inverse and normal primary creep transients are observed under conditions when $n \approx 3$ and 5, respectively [48]. In this case, it has been suggested that the solute atoms create drag forces on the mobile dislocations in the $n \sim 3$ region so that dislocation glide is impeded and becomes slower than dislocation climb [49]. In the regions corresponding to $n \sim 5$, dislocation climb becomes the rate-controlling mechanism since it becomes slower than the viscous glide process.

Although the observations shown in Fig. 10 are consistent with the expected behavior for a solid solution alloy, such as Al-5%Mg, a close examination of Fig. 7 fails to reveal the expected transition in the stress exponent from 5 to 3 to 5. It is important to note that some solid solution alloys, such as Cu-30%Zn [38], also fail to exhibit this transition although other characteristics of class A behavior have been observed in stress change tests. However, the nature of the creep transient behavior observed after repeated stress changes from 40 to 50 MPa and back at 900 K (Fig. 6) reveals that NiAl exhibits the characteristics of class A behavior only under low deformation strains and class M behavior at large values of strain. As noted earlier, the uninterrupted tests under similar stress and temperature conditions result in inverse primary

creep. These observations indicate that the inverse primary creep behavior, while due to an initial low mobile dislocation density, is not indicative of the typical class A response observed during steady-state creep of Al-5% Mg and other similar solid solution alloys involving solute locking of mobile dislocations in the $n \sim 3$ region.

Comparisons of primary creep behavior under compression and tension loading

Figure 11 superimposes the regions of the σ_e -T space, where inverse and normal primary creep occur under compression and tension loading for as-cast and extruded polycrystalline NiAl with similar grain sizes. In this case, the compression curves were generated on as-cast and extruded near-stoichiometric NiAl with a grain size of about 35 μm for which the $\dot{\epsilon}$ - σ data are reported elsewhere⁴ [14]. The region where inverse primary creep occurs under each type of loading is depicted by the shaded area in each case. The role of cracks and cavitation on the tensile creep behavior was judged to be small for two reasons: (a) the microstructures of longitudinal sections did not generally show any significant damage outside the immediate vicinity of the fractured area [50], and (b) the observations shown in Fig. 11 relate to the initial stages of creep, where damage accumulation is expected to be negligible. An examination of Fig. 11 reveals that inverse primary creep occurs at higher stresses and higher temperatures in compression than under tension loading. This interesting and important observation suggests that the factor(s) influencing dislocation mobility in NiAl is asymmetric in nature.

⁴ The datum point shown at 800 K under an initial stress of 250 MPa in Fig. 11 was obtained from a constant load creep test. It is not depicted in $\dot{\epsilon}$ - σ data reported in [14].

Examination of the role of impurities on dislocation mobility

Two characteristics of the transition from inverse to normal primary creep behavior should be noted. First, as shown in Figs 4 and 10, the nature of this transition is stress dependent at a constant temperature. The effect of increasing the stress is to activate a larger number of dislocation sources, increase the density of mobile and immobile dislocations as well as lower the activation energy for thermally-activated dislocation motion. Second, the fact that the inverse primary creep behavior is only observed in an intermediate stress and temperature regime (Fig. 10) indicates that the process is thermally activated and inconsistent with the operation of an athermal process, such as dislocation nucleation. A close examination of Figs. 4 reveals that there is a sharp drop in the creep rate soon after loading due to rapid work hardening with no significant recovery. This observation indicates that most of the dislocations that were generated at the commencement of creep were immobilized within a short period of time at these stresses and temperatures. Creep proceeds only when the mobility of the dislocations increases with time as recovery mechanisms become more predominant. As a result, it must be concluded that the observation of inverse primary creep is due to factors influencing dislocation mobility rather than those affecting dislocation generation.

As discussed earlier, dislocation mobility can be inhibited by the presence of interstitial or substitutional atoms. It is evident from Table 1 that the carbon content of the extrusion L 3176 was three times more than that of L 3175. The amounts of substitutional elements were determined to be insignificant in these two batches of material to be of relevance in influencing creep behavior. The nitrogen, oxygen and sulfur contents of the two extrusions were similar, and therefore, the role of these elements cannot be unambiguously separated. As mentioned earlier,

all the specimens tested at 700 and 800 K were obtained from L 3175, whereas those deformed at 900K and above were mainly machined from L 3176. However, in the few cases where specimens from both extrusions were crept at identical temperatures with a relatively small variation in the magnitude of the applied stress, no significant difference was observed other than the fact that the nature of the primary creep behavior was essentially dependent on stress and temperature. Also, Prakash and Pool [51] did not observe inverse primary creep in carbon-doped NiAl containing up to 0.2 at.% of C in the temperature range 973 to 1173 K under an initial compressive stress of 74.5 MPa. Instead, only normal primary creep was observed in all instances. Indirect evidence that carbon does not influence the shape of the primary creep curve is evident in other reports. For example, a comparison of the compressive creep curve for cast and extruded NiAl ($d \approx 35 \mu\text{m}$) with that for powder metallurgy (PM) and extruded NiAl ($d \approx 23 \mu\text{m}$) crept at 1100 K under an initial stress of 40 MPa revealed, that while the PM material exhibited inverse primary creep transient, the as-cast alloy exhibited normal primary creep [14]. In this case, the carbon contents of the PM and the as-cast alloys were 110 and 350 at. ppm, respectively. Based on these arguments, the probability that the observations ^{of} inverse primary creep in NiAl was caused by impurity or substitutional atoms appears highly unlikely. ?

Examination of other factors inhibiting dislocation mobility

Factors other than impurity and solute atoms can influence dislocation mobility. These include the existence of high Peierls forces [40,41,42], locking of dislocation sources due to the presence of sessile decomposed edge dislocation components [47], dislocation jogs on screw dislocations [43,44,45] and dislocation interaction with “extrinsic obstacles” [43,44,45]. Recent microstructural observations suggest that the Peierls forces are small in NiAl above 143 K

[43,44,45], so that dislocation mobility is unlikely to be limited by these forces in this alloy. However, high resolution transmission electron microscopy (HRTEM) of deformed NiAl bicrystals revealed that the core of perfect $\langle 011 \rangle$ edge oriented dislocations decompose into two separate $\langle 001 \rangle$ edge dislocation segments under an applied stress at room temperature [47]. Atomistic calculations based on the embedded atom method (EAM) have confirmed that it is energetically favorable for a $\langle 011 \rangle$ edge dislocation to decompose into two $\langle 010 \rangle$ sessile edge components with one possessing an Al-rich dislocation core and the other composed of a Ni-rich dislocation core. Thus, the formation of these two $\langle 010 \rangle$ sessile edge dislocations inhibits dislocation glide mobility and locks the dislocations. It was suggested that the unlocking mechanism involves the cooperative climb of the two $\langle 010 \rangle$ edge segments at high temperatures with the climb of one segment leading to vacancy generation while the climb of the other leading to vacancy annihilation. However, this coupled climb of the two $\langle 010 \rangle$ edge dislocations and its sequential nature presents a serious difficulty in rationalizing the present experimental observations. First, since this mechanism would result in the two $\langle 010 \rangle$ dislocations climbing away from each other as creep proceeds with a corresponding increase in the vacancy diffusion distance, it is expected that the creep rate would continue to decrease with increasing strain or time and finally become immeasurable. In reality, neither NiAl single [20] nor polycrystals (Fig. 4) show this predicted creep hardening behavior thereby suggesting that this is not a viable unlocking mechanism. Second, the above climb-controlled unlocking mechanism is likely to be independent of whether the applied stress was compressive or tensile in nature owing to the coupled nature of the process. As demonstrated in Fig. 11, the creep behavior of NiAl appears to be asymmetrical in nature and extremely sensitive to the nature of the stress state. Similarly, the observed magnitudes of Q_c are close to 300 and 400 kJ mol⁻¹ in regime II in compression and

tension tests, respectively (Fig. 12). Clearly, the coupled climb mechanism would lead to a unique value of Q_c depending on the slowest diffusion species.

If instead, it is assumed that the climb of these edge dislocations are decoupled, and hence independent processes, the observed differences in creep behavior in compression and tension tests can be qualitatively rationalized. In this case, the climb of each $\langle 010 \rangle$ dislocation can occur with the aid of Al vacancies, V_{Al} , and Ni vacancies, V_{Ni} , diffusing to the dislocation core, as described later in the paper, thereby providing a means of unlocking the dislocations.

An alternative locking mechanism proposed by Caillard *et al.* [43,44,45] involves the locking of screw dislocations by jogs, dipoles and prismatic loops formed as segments of the same dislocation cross slips on different slip planes. Careful in-situ transmission electron microscopy (TEM) studies of NiAl single crystals have confirmed the occurrence of this mechanism at room temperature. Although proposed for low temperature deformation, the Caillard model [43,44,45] is also consistent with both the experimental observations reported here and in the literature on the high temperature creep of near-stoichiometric NiAl especially under conditions corresponding to regime III in Fig. 9 [1,7,13]. First, the experimental values of V^* varying between 50 and 350 b^3 [1,13,5] fall within the expected range of values for the cross-slip of jogged screw dislocations [35,36]. Second, the stress dependence of the activation energy described by equation (6(a)) is consistent with both the jog-pair as well as the compact cross-slip models which describe the exact manner in which the cross-slip screw dislocations occur [37]. Third, TEM observations of crept NiAl specimens have confirmed the occurrence of cross-slip of screw dislocations [7,19] along with the observations of jogs, dipoles and prismatic loops

[7,8,11,12,19]. Despite this consistent agreement between the experimental results and the cross-slip models, it should be noted that the magnitudes of V^* , as well as the fact that the stress dependence of Q_c given by eqn. (4) is equally probable, are also consistent with other dislocation glide mechanisms, such as obstacle-controlled glide [35,36].

No microstructural observations have been reported in the literature describing the progressive evolution of the dislocation substructure in polycrystalline NiAl as a function of creep strain under stress and temperature conditions where inverse and normal primary creep are observed. Nevertheless, it is attractive to assume that the cross-slip of screw dislocations along with the associated jog and dipole formation occur during the early stages of primary creep of NiAl under all stresses and at all temperatures due to the consistency of this concept with the experimental observations reported here. As discussed in the previous paragraph, this concept is also consistent with other characteristics associated with the creep of NiAl. It is noted that Xu and Arsenault [5] have proposed a generic model for the high temperature deformation of NiAl under constant engineering compression strain rate assuming that long screw dislocations are pinned at jogs. However, their model does not consider the role of specific defects that could influence the deformation of this intermetallic alloy. In addition to the locking of the screw dislocations by edge-oriented jogs, dipoles and prismatic loops, the observations of Caillard *et al.* [43,44,45] suggest that other “extrinsic” obstacles, which are too small to be resolved by TEM, can also act as pinning points at the jogs. In this case, it is hypothesized that these pinning points could be defect complexes, such as antistructure defects, Al_{Ni} and Ni_{Al} and triple point defects consisting of two Al or Ni vacancies and one Al_{Ni} or Ni_{Al} defect, respectively. At low temperatures, the dislocation can break away from the pinning points when the shear stress, τ ,

acting on it exceeds $F_c/\lambda b$, where F_c is the critical force required to cause the dislocation to break away from weak extrinsic obstacles, λ is the average distance between obstacles along a screw dislocation and b is the Burgers vector [45]. At high temperatures, diffusional processes, such as dislocation climb and the diffusion of the antistructure and triple defects away from the dislocation core, can also result in unlocking of the jogged screw dislocations.

Compression and tension creep asymmetry

As shown in Fig. 11, the primary creep response of NiAl is asymmetrical in compression and tension creep. This asymmetry is also observed when the experimental values of Q_c determined in compression and tension tests in regime II are compared with each other (Fig. 12). In this case, the horizontal line represents the value of $Q_{Ni}^* \approx 290 \text{ kJ mol}^{-1}$ based on experimental measurements of the activation energy for tracer diffusion of Ni in stoichiometric NiAl [31]. It is clear from Fig. 12 that the values of Q_c obtained in compression in regime II are similar to the experimental values of Q_{Ni}^* [30,31] irrespective of the method used to process the extrusions, whereas the magnitude of Q_c of about 400 kJ mol^{-1} determined from the tension tests is about 100 kJ mol^{-1} higher than that observed in the compression tests. However, the magnitudes of Q_c vary between 250 and 275 kJ mol^{-1} in regime III irrespective of loading and processing conditions although it is likely that the boundary between regimes II and III may have moved to higher stresses for the cast and extruded material crept in compression. If it is assumed that the same diffusion species controls tensile creep of near-stoichiometric NiAl, and noting that the magnitude of Q_c in regime III is 0.63 of that in regime II, it is likely that dislocation climb is aided by pipe diffusion in regime III and lattice diffusion in regime II.

Figure 13 compares the $\dot{\epsilon}$ - σ plots for as-cast and extruded near-stoichiometric NiAl crept at identical temperatures in compression [15] and tension, where the specimens had similar grain sizes. The broken and solid lines represent the regression lines through the compression and tension data, respectively. A close examination of Fig. 13 suggests two major differences in these two sets of data. First, the material creeps at significantly faster rates in tension creep than in compression creep especially at the lower temperatures, where the creep rates often vary by several orders of magnitude for $T < 1000$ K and $\sigma > 40$ MPa. Some degree of convergence of the two sets of data is evident at 1000 and 1100 K when the stresses are low. Second, $n \approx 5$ for the compression data between 900 and 1200 K for $\sigma > 10$ MPa and only increases to about 13 at 800 K. In contrast, as noted earlier, $n \approx 5-6$ when $T \geq 1000$ K for $\sigma < 40$ MPa and $n > 8.5$ when $T \leq 1000$ K for $\sigma > 40$ MPa (Table 3).

Comparison of stress exponents and activation energies for creep with literature data

Table 5 compares the values of n and either the apparent activation energy for creep, Q_a , or Q_c observed in the present investigation with those reported in the literature for near-stoichiometric single and polycrystalline NiAl. It should be noted that Table 5 does not include values Q_a , or Q_c , which were stress dependent [1,7,11,13]. Correcting for the temperature dependence of E based on eqn. (3), the estimated values of Q_c for the literature data shown in Table 5 are usually between 0.5 and 3% of Q_a ; thus, $Q_a \sim Q_c$. The magnitudes of n observed in the present study fall within the range of values observed in the other investigations. In an earlier paper [15], it was pointed out that the published values of n for polycrystalline NiAl appear to fall within two broad categories in a similar range of stresses and temperatures: (a) fine-grained NiAl with $d < 40$ μm exhibit values of $n \approx 5.0$ to 7.5; (b) coarse-grained NiAl with $d > 150$ μm

often exhibit values of $n \approx 3.5$ to 4.5 . More direct evidence in support of this observation has been reported by Artz and Grahle [14,16], who observed that $n \approx 4.5$ for NiAl specimens with $d \approx 170 \mu\text{m}$ and $n \approx 7.3$ for specimens with $20 \mu\text{m}$. It has been suggested that fine-grained NiAl exhibits higher values of the stress exponent because the equilibrium subgrain size exceeded the grain size thereby resulting in a “constant structure” flow behavior [2,3,16]. More recently, it was noted that this argument is inconsistent with the experimental observations [24,25]. Table 5 also shows that the observed values of Q_a or Q_c for NiAl vary over a wide range from 230 to 565 kJ mol^{-1} , where the data generally fall into two categories: (a) Q_a or $Q_c \leq 300 \text{ kJ mol}^{-1}$ and (b) Q_a or $Q_c \geq 320 \text{ kJ mol}^{-1}$ irrespective of the loading mode.

Comparison of the activation energy for creep in regime II with diffusion results

The magnitude of $Q_c \approx 300 \text{ kJ mol}^{-1}$ observed in regime II during compression creep (Fig. 12) can be reasonably identified with that associated Q_{Ni}^* in NiAl [30,31]. In contrast, since the atomic volumes of Al and Ni are 1.7×10^{-29} and $1.1 \times 10^{-29} \text{ m}^3$ with Al being the larger atom [52], it is reasonable to expect that the higher value of $Q_c \approx 400 \text{ kJ mol}^{-1}$ observed in regime II during tension creep corresponds to the activation energy for lattice diffusion of Al in NiAl. However, direct measurements of the tracer diffusivity of Al, D_{Al}^* , in NiAl have not been reported due to the absence of a suitable radioactive tracer. Recently, Nakamura *et al.* [34] estimated the magnitude of D_{Al}^* in Ni-43.4Al from the Darken-Manning relation [53,54] using Ni tracer diffusion literature data, D_{Ni}^* , and the measured interdiffusion coefficient, \tilde{D} , in the alloy. Attempts to estimate the activation energy for tracer diffusion of Al, Q_{Al}^* , from published data [31,33] for near-stoichiometric NiAl in a similar manner resulted in values of Q_{Al}^* varying

between 355 and 430 kJ mol⁻¹ for $\Phi S = 0.01$ to 0.25⁵, where Φ is the thermodynamic factor and S is the vacancy wind factor. However, these calculations were unreliable in part due to uncertainties in the magnitudes of Φ and in part due to discrepancies in using experimental diffusion data from different investigations. Alternatively, D^*_{Al} can be estimated directly from the relationship $D^*_{Al} = D^*_{Ni}(D_{Al}/D_{Ni})$, where D_{Al} and D_{Ni} are the intrinsic diffusion coefficients of Al and Ni, respectively. Using an experimental value of $D_{Al}/D_{Ni} \sim 0.3$ [32], and assuming it to be independent of temperature, the estimated values of Q^*_{Al} were 290 and 307 kJ mol⁻¹ for values of D^*_{Ni} reported by Frank *et al.* [31] and Hancock and McDonnell [30], respectively. These estimates of Q^*_{Al} are much lower than the experimental value of $Q_c \approx 400$ kJ mol⁻¹, and once again, they are sensitive to variations in the diffusion data published in the literature. It is also worth noting that Kim and Chang [33] have suggested that the Darken-Manning equation cannot be applied to highly ordered intermetallic compounds like NiAl.

In the absence of a reliable way of estimating or measuring Q^*_{Al} , it is necessary to compare the creep activation energy data with theoretical estimates of the activation energies for the lattice diffusion of Al and Ni vacancies, Q_{Al} and Q_{Ni} , respectively, in NiAl [55,56]. The experimental values of Q_c observed in regimes II and III during compression [11,13,15] and tension creep are compared in Table 6 with the calculated values of activation energy for self-diffusion involving the diffusion of Al and Ni vacancies for several probable diffusion mechanisms [31,55,56]. Details of these diffusion mechanisms are discussed elsewhere [31,55,56]. An examination of Table 6 shows that the four-ring (4R) mechanism predicts very high activation energies for diffusion, which is not observed in both diffusion [30,31,32,33,34] as

⁵ It should be noted that values of $\Phi S > 0.25$ resulted in negative values of D^*_{Al} .

well as in creep experiments (Table 5). Therefore, Mishin and Farkas [55] concluded that this mechanism is unimportant in diffusion in NiAl. Similarly, its importance in governing the creep of NiAl can be ruled out. The anti-structure bridge (ASB) mechanism is expected to be important only in the Ni-rich NiAl when the Ni anti-structure defects exceed 5% [31]. Thus, its importance in transferring Ni vacancies through the near-stoichiometric NiAl lattice to the dislocation core in order to aid dislocation climb during creep is expected to be insignificant. The next nearest neighbor (NNN) mechanism predicts $Q_{Al} \approx 285 \text{ kJ mol}^{-1}$ [55,56], which is in reasonable agreement with the value of $Q_c \approx 300 \text{ kJ mol}^{-1}$ observed for the compression creep data in regime II (Fig. 12 & Table 6). However, the value of $Q_{Ni} \approx 265 \text{ kJ mol}^{-1}$ predicted for Ni diffusion by the NNN mechanism deviates from the experimental value of $Q_c \approx 300 \text{ kJ mol}^{-1}$ by over 10%. The triple defect (TD) and the six jump cycle (6JC(V_{Ni})) mechanisms involving the diffusion of Ni vacancies, which predict $Q_{Ni} \approx 300 \text{ kJ mol}^{-1}$, also agree with $Q_c \approx 300 \text{ kJ mol}^{-1}$ observed in compression creep tests (Fig. 12 & Table 5). Only the 6JC(V_{Al}) mechanism involving the diffusion of Al vacancies predicts a value of $Q_{Al} \approx 365 \text{ kJ mol}^{-1}$, which is within 10% of the experimental value of $Q_c \approx 400 \text{ kJ mol}^{-1}$ observed in regime II during tensile creep (Fig. 12). Theoretical calculations suggest that the activation volumes for diffusion are much larger for the two 6JC mechanisms than for ASB, which implies that they are extremely sensitive to hydrostatic stresses than the ASB mechanism [56,57]. Although the magnitudes of the creep activation energies as well as their sensitivity to the nature of the stress state are in reasonable agreement with the predicted diffusion mechanisms (Table 6), it is noted that a hydrostatic stress state exists only in the vicinity of the dislocation core in specimens deformed under uniaxial loading.

Based on the above discussion, it is reasonable to rule out the role of the ASB, NNN and the TD mechanisms in governing tensile creep results observed in regime II. Only the 6JC(V_{Al}) mechanism predicts a value of Q_{Al} consistent with the present observations. However, the value of Q_{Al} predicted by the NNN process as well as the calculated values of Q_{Ni} for the TD and 6JC(V_{Ni}) mechanism are all in reasonable with the compression creep data observed in regime II, and it is not possible to unambiguously identify which of these three diffusion mechanisms is important during compression creep of near stoichiometric NiAl.

Phenomenological interpretation of regime III

Figure 9 suggests that $Q_c \approx 250 \text{ kJ mol}^{-1}$, which is about 0.63 of that measured in regime II, for the tension data in regime III. As discussed in the last section, the rate controlling mechanism in regime II presumably involves the diffusion of Al vacancies through the lattice. Therefore, it is reasonable to conclude that regime III is controlled by dislocation core diffusion of Al vacancies. Noting that $Q_c = 365 \text{ kJ mol}^{-1}$ for the 6JC(V_{Al}) lattice diffusion mechanism [56] (Table 6), the predicted value for dislocation core diffusion of Al vacancies is about 230 kJ mol^{-1} assuming that its magnitude is 0.63 of that for lattice diffusion. This value is reasonably close to the experimental results shown in eqn. 7(b) and Fig. 9. However, the interpretation of the compression results in regime III in a similar manner is unsatisfactory since the predicted value for dislocation core diffusion of Ni vacancies is about 190 kJ mol^{-1} assuming that the lattice diffusion of Ni vacancies is by the 6JC(V_{Ni}) mechanism.

However, a consistent picture emerges if it is assumed that the vacancies flow to the dislocations also occurs through the lattice as in regime II but by a different mechanism. A

comparison of the predicted activation energies for diffusion with the experimental data (Table 6) suggests that the Al or Ni vacancy flow occur by the 6JC mechanism in regime II and by the NNN process in regime III under tensile or compressive creep, respectively. The predicted activation volume for the NNN mechanism is less than that for the 6JC process [56] so that Q_c is expected to be less dependent on the nature of the stress state, which is consistent with the observations shown in Fig. 9.

Mechanistic of dislocation climb in near-stoichiometric NiAl

Earlier on, it was suggested that the Caillard model [43,44,45], originally proposed for low temperature deformation of NiAl, could be equally applicable to high temperature creep. At high temperatures, it is envisioned that the pinning or unpinning of jogs on screw dislocations involves the diffusion of defect complexes to or from the dislocation core, respectively, thereby resulting in the climb of the jog. The non-conservative motion of a jog on a screw dislocation is a two step process involving the transport of vacancies to the jog followed by its absorption into the dislocation core to permit dislocation climb. The slowest of these two steps would control creep in NiAl and influence the magnitude of Q_c . The diffusion mechanisms discussed in the previous section deal with the first step of transporting the Al or Ni vacancies either through the lattice or along the dislocation core to the jog but shed little light on the atomic processes involved in its subsequent climb.

Figure 14(a-i) schematically illustrates the how the 6JC process can occur in the vicinity of a $\langle 100 \rangle (010)$ dislocation core, where the dislocation line lies along a cube orientation and the open and solid circles represent the Ni and Al atoms, respectively. The atomic positions for these

types of dislocations in NiAl were previously determined from atomistic modeling studies, where it was determined that the relaxed dislocation core structure in NiAl can be represented by inserting one extra half plane consisting of one type of atoms between two symmetrically branched planes of the other type of atoms [58]. The insertion of an Al half plane between two symmetrically branched Ni planes leads to a slightly lower energy configuration than when a Ni half plane is inserted between Al planes by about 38 kJ mol^{-1} . For simplicity, it is assumed that an Al or a Ni vacancy enters the dislocation core by the NNN mechanism (Fig. 14(a)). It should be noted that the dislocation core consists of one type of atoms as indicated by the broken inverse triangle. Ternes *et al.* [58] have calculated the energy changes resulting from placing either an Al vacancy or a Ni antisite defect at different points around the dislocation core for unstressed NiAl. These calculations reveal that Al vacancies are attracted to the cores of both the $\langle 100 \rangle \{010\}$ and $\langle 100 \rangle \{011\}$ dislocations, where the energy is lower above the slip plane than below it. The application of an applied stress would change the nature of this dislocation-vacancy interaction through its influence on the total energy of the dislocation core. A tensile hydrostatic stress would result in a dilation of the dislocation core and increase the probability that the larger Al vacancy can participate in the climb, whereas a compressive hydrostatic stress would compress the core and decrease the probability of its participation. Molecular dynamic calculations are required to demonstrate the effect of a compressive or tensile hydrostatic stress on the energetics of the dislocation-vacancy interaction during creep.

Figures 14(b-h) schematically show the sequence of atom-vacancy⁶ jumps and the relative positions of three atoms designated as 1, 2 and 3 through the different stages of 6JC. Again, it is assumed that the vacancy exits the dislocation core by the NNN mechanism (Fig. 14(h)) thereby leading to the final configuration shown in Fig. 14(i). A comparison of Figs. 14(a) and (i) reveals that atoms 1 and 3 have interchanged positions and atom 2 has moved from right to left after the completion of the 6JC.

An alternative and simpler atom-vacancy exchange process facilitating dislocation climb in NiAl can be envisioned if the NNN mechanism is operative. For the dislocation core structure shown in Fig. 15(a), it can be envisioned that atoms 1 and 2 exchange positions with vacancies A and B, respectively, residing on the NNN site (Fig. 15(a)). Next, atom 4 exchanges positions with vacancy A and atom 5 with vacancy B. The final configuration is shown in Fig. 15(b) after atom 6 exchanges position with vacancy A assuming that there is no lattice relaxation.

SUMMARY AND CONCLUSIONS

Long term tensile creep tests were conducted on near-stoichiometric NiAl between 700 and 1200 K and their behavior were compared with previously published compression creep data on material with a similar grain size and processing history [15,24,25]. Inverse and normal primary creep occurs in both modes of deformation, where the former type of transient behavior was observed at higher stresses and higher temperatures under compression than in tension loading. Several possibilities limiting dislocation mobility in NiAl were examined and it was

⁶ It is reasonable to expect that the site occupancy restrictions that apply in the lattice far away from the dislocation core are likely to be relaxed in the close vicinity of the dislocation core due to the distorted nature of the lattice.

concluded that models postulating the non-conservative motion of jogs on screw dislocations are the most consistent with the present observations. It is suggested that diffusion of defect complexes, such as antistructure and triple defects, to and from the dislocation core, ~~thereby~~ leading^s to the pinning and unpinning of the jogs.

The stress exponents for tensile creep varied between 4.9 and 13.9 with the values of $n \sim 5-6$ varying between 1000 and 1200 K and $n > 8.5$ between 700 and 1000 K. Four deformation regimes were identified. The true activation energy was observed to be less than that for lattice diffusion of Ni tracers in regime I. The true activation energy for tensile creep in regime II was determined to be about 400 kJ mol^{-1} for $20 \leq \sigma \leq 50 \text{ MPa}$ and 250 kJ mol^{-1} in regime III for $50 \leq \sigma \leq 110 \text{ MPa}$. The activation energy exhibited an inverse stress dependence in accordance with both obstacle glide and compact cross-slip controlled creep mechanisms in regime IV. The values of 400 and 250 kJ mol^{-1} observed in regime II and III, respectively, were attributed to the lattice diffusion of Al vacancies based on values predicted by diffusion models for NiAl. In comparison, the measured activation energies for compressive creep of 300 kJ mol^{-1} in regime II is in reasonable agreement with the experimental values reported for lattice self diffusion of Ni tracers in NiAl as well as with the calculated values for the lattice diffusion of Ni vacancies in NiAl. Finally, the mechanistic of dislocation climb in NiAl is discussed based on the next nearest neighbor and the six jump cycle atom-vacancy exchange mechanisms occurring within the core of jog on a screw dislocation.

ACKNOWLEDGEMENTS

The author thanks Dr. J. Daniel Whittenberger for reviewing this paper and for his comments and suggestions. He also thanks Profs. Ali Argon and Diana Farkas for the useful discussions he had with them during the course of this investigation. Mr. Pete Eichele and Mr. Tom Monihan conducted the creep tests and their help is gratefully acknowledged. Partial support for this study was provided by the Wright-Patterson Air Force Base.

REFERENCES

1. R. R. Vandervoort, A. K. Mukherjee and J. E. Dorn: *Trans. ASM*, 1966, vol. 59, pp. 930-44.
2. J. D. Whittenberger: *J. Mater. Sci.*, 1987, vol. 22, pp. 394-402.
3. J. D. Whittenberger: *J. Mater. Sci.*, 1988, vol. 23, pp. 235-240.
4. J. D. Whittenberger: *Effect of Grain Size on the High Temperature Properties of B2 Aluminides*, NASA TM 101382, Lewis Research Center, Cleveland, 1987, pp. 1-24.
5. K. Xu and R. J. Arsenault: *Acta Mater.*, 1999, vol. 47, pp. 3023-3040.
6. W. Yang, R. A. Dodd and P. R. Strutt: *Metall. Trans.*, 1972, vol. 3, pp. 2049-2054.
7. W. J. Yang and R. A. Dodd: *Met. Sci. J.*, 1973, vol. 7, pp. 41-47.
8. P. R. Strutt, R. S. Polvani and B. H. Kear: *Scripta Metall*, 1973, vol. 7, pp. 949-954.
9. A. Prakash and R. A. Dodd: *J. Mater. Sci.*, 1981, vol. 16, 2495-2500.
10. M. Rudy and G. Sauthoff: *Mater. Sci. Eng.*, 1986, vol. 81, 525-30.
11. S. V. Raj and S. C. Farmer: in *High-Temperature Ordered Intermetallic Alloys V*, I. Baker, R. Darolia, J. D. Whittenberger and M. H. Yoo, eds., Materials Research Society, Pittsburgh, PA, 1993, vol. 288, pp. 647-652.
12. K. Sadananda, C. R. Feng, H. N. Jones and J. J. Petrovic: in *Proceeding of the First International Symposium on Structural Intermetallics*, R. Darolia, J. J. Lewandowski, C. T. Liu, P. L. Martin, D. B. Miracle and M. V. Nathal, eds., The Minerals, Metals and Materials Society, Warrendale, PA, 1993, pp. 809-818.
13. S. V. Raj and S. C. Farmer: *Metall. Mater. Trans. A*, 1995, vol. 26A, pp. 343-356.

14. E. Artz and P. Grahle: in *High-Temperature Ordered Intermetallic Alloys VI*, J. Horton, I. Baker, S. Hanada, R. D. Noebe and D. S. Schwartz, eds., Materials Research Society, Pittsburgh, PA, 1995, vol. 364, pp. 525-536..
15. S. V. Raj, A. Garg and T. R. Bieler: in *High-Temperature Ordered Intermetallic Alloys VII*, C. C. Koch, C. T. Liu, N. S. Stoloff and A. Wanner, eds., Materials Research Society, Pittsburgh, PA, 1997, vol. 460, pp. 473-478.
16. E. Artz and P. Grahle: *Acta Mater.*, 1998, vol. 46, pp. 2717-2727.
17. T. A. Venkatesh and D. C. Dunand: *Metall. Mater. Trans. A*, 2000, vol. 31A, pp. 781-792.
18. P. R. Strutt and R. A. Dodd: in *Ordered Alloys: Structural Applications and Physical Metallurgy*, B. H. Kear, C. T. Sims, N. S. Stoloff and J. H. Westbrook, eds., Claitor's Publishing Division, Baton Rouge, LA, 1970, pp. 475-504.
19. W. R. Kanne, P. R. Strutt and R. A. Dodd: *Trans. AIME*, 1969, vol. 245, pp. 1259-1267.
20. K. R. Forbes, U. Glatzel, R. Darolia and W. D. Nix: *Metall. Mater. Trans. A*, 1996, vol. 27A, pp. 1229-1240.
21. J. D. Whittenberger and R. D. Noebe, unpublished research, NASA Lewis Research Center, Cleveland, OH (1991).
22. L. A. Hocking, P. R. Strutt and R. A. Dodd: *J. Inst. Metals*, 1971, vol. 99, pp. 98-101.
23. J. Bevk, R. A. Dodd and P. R. Strutt: *Metall. Trans.*, vol. 4, 1973, pp. 159-166.
24. S. V. Raj: in *Creep Deformation: Fundamentals and Applications*, R. S. Mishra, J. C. Earthman and S. V. Raj, eds., The Minerals, Metals & Materials Society, Warrendale, PA, 2002, pp. 351-360.

25. S. V. Raj: "Creep Behavior of Near-Stoichiometric Polycrystalline Binary Alloy", NASA TM-2002-211210, Glenn Research Center, Cleveland, OH (2002).
26. R. C. Gifkins: J. Inst. Metals, 1957, vol. 86, pp. 15-16.
27. M. S. Soliman, T. J. Ginter and F. A. Mohamed: Phil. Mag. A, 1983, vol. A 48, pp. 63-81.
28. A. K. Mukherjee, J. E. Bird and J. E. Dorn: Trans. ASM, 1969, vol. 62, pp. 155-179.
29. M. R. Harmouche and A. Wolfenden: J. Testing. Eval., 1987, vol. 15, pp. 101-04.
30. G. F. Hancock and B. R. McDonnell: Phys. Status Solidi, 1971, vol. 4(a), pp. 143-50.
31. St. Frank, S. V. Divinski, U. Södervall and Chr. Herzig: Acta Mater., 2001, vol. 49, pp. 1399-1411.
32. S. Shankar and L. L. Seigle: Metall. Trans. A, 1978, vol. 9A, pp. 1467-1476.
33. S. Kim and Y. A. Chang: Metall. Trans. A, 2000, vol. 31A, pp. 1519-1524.
34. R. Nakamura, K. Takasawa, Y. Yamazaki and Y. Iijima: Intermetall., 2002, vol. 10, pp. 195-204.
35. H. Conrad: JOM, 1964, vol. 16, pp. 582-588.
36. A. G. Evans and R. D. Rawlings: Phys. Status Solidi, 1969, vol. 34, pp. 9-31.
37. W. Püschl: Prog. Mater. Sci., 2002, vol. 47, pp. 415-461.
38. S. V. Raj: J. Mater. Sci., 1991, vol. 26, pp. 3533-3543.
39. H. Oikawa, N. Kuriyama, D. Mizukoshi and S. Karashima: Mater. Sci. Eng., 1977, vol. 29, pp. 131-135.
40. J. Weertman: J. Appl. Phys., 1957, vol. 28, pp. 1185-1189.
41. P. Haasen: in *Dislocation Dynamics*, A. R. Rosenfield, G. T. Hahn, A. L. Bement, Jr. and R. I. Jaffee, eds., McGraw-Hill Book Company, New York, NY, 1967, pp. 701-722.

42. U. Messerschmidt, R. Haushälter and M. Bartsch: Mater. Sci. Eng., 1997, vol. A 234/236, pp. 822-825.
43. D. Caillard: in *High-Temperature Ordered Intermetallic Alloys VIII*, E. P. George, M. Yamaguchi, and M. J. Mills, eds., Materials Research Society, Pittsburgh, PA, 1999, vol. 552, pp. KK9.9.1-KK9.9.7.
44. D. Caillard, C. Vailhé and D. Farkas: Phil. Mag. A, 1999, vol. 79, pp. 723-739.
45. D. Caillard and A. Couret: Mater. Sci. Eng., 2002, vol. A 322, pp. 108-117.
46. F. A. Mohamed: Mater. Sci. Eng., 1983, vol. 61, pp. 149-165.
47. M. J. Mills, J. E. Angelo, M. S. Daw, J. D. Weinburg and D. B. Miracle: Mater. Sci. Eng., 1993, vol. A192/193, pp. 134-141.
48. P. Yavari and T. G. Langdon: Acta Metall., 1982, vol. 30, pp. 2181-2196.
49. T. Endo, T. Shimada and T. G. Langdon: Acta Metall., 1984, vol. 32, pp. 1991-1999.
50. S. V. Raj, unpublished research, (1995), Glenn Research Center, Cleveland, OH.
51. A. Prakash and M. J. Pool: J. Mater. Sci., 1981, vol. 16, pp. 2495-2500.
52. H. W. King: J. Mater. Sci., 1966, vol. 1, pp. 79-90.
53. L. S. Darken: Trans. AIME, 1948, vol. 175, pp. 184-201.
54. J. S. Manning: Acta Metall., 1967, vol. 15, p. 817.
55. Y. Mishin and D. Farkas: Phil. Mag., 1997, vol. 75, pp. 187-199.
56. Y. Mishin and D. Farkas: Scripta Mater., 1998, vol. 39, pp. 625-630.
57. D. Farkas, private communication, 2002.
58. K. Ternes, Z. Y. Xie and D. Farkas: Mater. Sci. Eng., 1995, vol. 192/193, pp. 125-133.

Table 1.: Chemical composition (at.%) and initial grain sizes of the two extruded NiAl rods.

Extrusion I.D.	Extrusion conditions	Al	C	N	Ni	O	d (μm)
L 3175	1400 K; 16:1	49.8	0.0090	0.0005	50.2	0.0110	38.7 ± 2.5
L 3176	1400 K; 20:1	50.6	0.0270	0.0010	49.4	0.0120	38.6 ± 2.3

Table 2: Test conditions and final grain sizes for several specimens after long term testing.

Region	T (K)	σ (MPa)	ϵ (%)	t_r (h)	d_f (μm)	Sample size
shoulder	700	100	0.0	6529.4	65.7 ± 5.3	210
gage	700	100	8.4	6529.4	67.0 ± 3.9	749
shoulder	700	120	0.0	2413.6	62.9 ± 7.9	266
gage	700	120	53.4	2413.6	54.2 ± 4.2	888
shoulder	1100	10	0.0	6693.5	98.0 ± 18.8	114
gage	1100	10	4.0	6693.5	150.6 ± 9.6	533
shoulder	1200	10	0.0	9114.2	195.4 ± 31.1	86
gage	1200	10	4.3	9114.2	199.6 ± 15.0	367
shoulder	1200	13	0.0	326.6	162.6 ± 11.7	106
gage	1200	13	55.8	326.6	168.2 ± 25.4	264

Table 3.: Values of A , n and R_d^2 observed in tension creep of NiAl at different temperatures.

T (K)	σ (MPa)	n	A_1 (MPa⁻ⁿ s⁻¹)	R_d^2
700	100-170	13.9	3.3×10^{-37}	0.946
800	75-145	8.7	3.1×10^{-24}	0.992
900	40-80	13.2	7.4×10^{-31}	0.894
1000	25-35	5.1	7.4×10^{-16}	0.664
1000	35-65	12.3	9.3×10^{-28}	0.968
1100	10-40	6.1	1.0×10^{-15}	0.891
1200	10-25	4.9	7.7×10^{-13}	0.902

Table 4.: Activation energies for creep at different values of true stress.

σ (MPa)	Q_c (kJ mol ⁻¹)	R^2_d
15.9	302.5	-
21.3	237.9	-
25.7	387.9 ± 20.8	0.997
40.3	414.0 ± 39.7	0.993
50.2	341.0 ± 29.4	0.994
60.9	231.7 ± 14.2	0.992
76.2	259.4 ± 4.8	0.999
100.0	260.7	-
120.0	244.0	-
150.0	175.7	-

Table 5. Values of the creep stress exponent and stress-independent activation energy observed in near-stoichiometric polycrystalline and single crystalline NiAl.

Year	Al (at. %)	Processing	Testing Mode ^(a)	d (μm)	T (K)	n	Q _a or Q _c (kJ mol ⁻¹)	Ref.
1966	49.6	Cast	CSR; C	1130	1073- 1748	3.3 - 6.9	290 ^(b)	[1]
1969	50.4	Directional solidification & homogenized at 1523-1573 K/ 48 h	CL; T	Several <hkl> SX	748- 1048	-	310 ^(b)	[19]
1971	50.4 ^(c)	Directional solidification & homogenized at 1523-1573 K/ 48 h	CL; C	<123> SX	1023- 1223	5.4- 7.7	300 ^(b)	[22]
1973	50.3	Cast & annealed at 1573 K (?)	CL; C	450	1073- 1318	4.6 - 10.2	285 ^(b)	[7]
1973	49.4	Cast & annealed at 1473 K/48 h: a) iced brine quench; b) aged at 973 K/48 h	CS; C	1015	1123- 1323	-	565 ^(b) 230 ^(b)	[8]
1973	50.1- 50.5	Directional solidification & homogenized at 1573 K	CL; T	<hkl> SX;	1023- 1328	4.0- 4.5	-	[23]
1985; 1986	50.0	Cast & annealed at 1473 K/24 h	CL; C	500-600	1173	4.7	-	[10]
1987	49.2- 50.6	PM-extruded	CSR; C	13-17	1200- 1400	5.5- 6.5	305- 310 ^(b)	[2]
1991	50.0	Modified Bridgman	CSR; C	<001> SX	1000- 1300	6.1	440 ^(b)	[21]
1993; 1995	50.6	PM-extruded	CL; C	23	1000- 1300	5.8- 7.4	290- 300	[11, 13]
1996	50.0	Bridgman technique & annealed at 1589 K/ 50 h	CS; T; CSR; C	[223]; [111]; [011]; [07 10]	1123- 1473	3.7- 9.0	320 ^(b)	[20]

				SX [001] SX		3.9- 11.4	320 ^(b)	
1998	50.4	PM-extruded; PM-extruded & annealed at 1723 K/50 h	CL; C	20; 170	1300- 1473; 1300- 1400	7.3; 4.5	290 ^(b) ; 300 ^(b)	[16]
1997	50.3	Cast & extruded	CL; C	35	800- 1200	4.9- 8.7	300	[15]
1999	NiAl ^(d)	Hot pressed	CSR; C	5	300- 1273	7.6	345 ^(b)	[5]
2000	NiAl ^(e)	Reactive infiltration	CL; C	200	988 & 1298	5.5 & 5.6	375 ^(b)	[17]
	49.8- 50.6	Cast & extruded	CL; T	39	700- 1200	4.9- 6.1 8.7- 13.9	400 (20 ≤ σ ≤ 50 MPa); 250 (50 ≤ σ ≤ 110 MPa)	This study

- a) C = compression; CL = constant load; CS = Constant stress; CSR = constant strain rate; T = tension;
- b) Apparent activation energy reported. The true activation energies incorporating the correction for the shear modulus will be lower in value.
- c) Values of n and Q_c were estimated from the published data.
- d) The exact composition of the tested specimens was not reported.
- e) The reactive infiltrated ingot showed a linear variation in the Al content from about 36 to 47 (at.%) for a linear traverse of about 27 mm along the ingot.

Table 6. Comparison of the true activation energies for compression and tensile creep of NiAl with those predicted for lattice self-diffusion of Al and Ni vacancies for several mechanisms.

Q_c (kJ mol ⁻¹) Compression	Q_c (kJ mol ⁻¹) Tension	Diffusion Mechanism	Q_{Al} (kJ mol ⁻¹)	Q_{Ni} (kJ mol ⁻¹)
300 [11,13,15]	400 ($20 \leq \sigma \leq 50$ MPa); 250 ($50 \leq \sigma \leq 110$ MPa) (present study)			
		Triple Defect (TD)	-	300 [31]
		Four Ring (4R)	835 [55]	835 [55]
		Next Nearest Neighbor (NNN)	285 [55]	265 [55,56]
		Six Jump Cycle (6JC)	365 [56]	300 [56]
		Anti-structure Bridge (ASB)	-	255 [56]

FIGURE CAPTIONS

Fig. 1: Optical micrographs of the (a) longitudinal and (b) transverse sections of the as-extruded rods.

Fig. 2: Creep specimen designs used for tension tests; (a) smooth, and (b) & (c) ridged specimens.

Fig. 3: Tensile true strain vs. time curves for near-stoichiometric NiAl at (a) 700 K, (b) 900 K and (c) 1200 K under initial applied stresses varying from 10 to 170 MPa showing inverse and normal primary creep behavior.

Fig. 4: Tensile true creep rate vs. true strain curves for near-stoichiometric NiAl at (a) 700 K, (b) 900 K and (c) 1200 K under initial applied stresses varying from 10 to 170 MPa showing inverse and normal primary creep behavior.

Fig. 5: Long term tensile creep curves observed between 700 and 1200 K under initial applied stresses varying from 10 to 100 MPa showing inverse, multiple and normal primary creep behavior.

Fig. 6: The shapes of the creep transients observed in a stress change experiment conducted at 900 K between engineering stresses of 40 and 50 MPa under conditions where inverse primary creep is observed: (a) Tensile true strain vs. time curves; (b)

tensile true creep rate vs. true strain curves; (c) tensile true creep rate vs. time curves. The true stresses before and after each stress change are indicated in (b) & (c).

Fig. 7: Tensile true creep rate vs. true stress plots for near-stoichiometric NiAl between 700 and 1200 K determined in the secondary creep region.

Fig. 8: Arrhenius plots for near-stoichiometric NiAl for true stresses varying between 15.9 MPa ($\sigma/E \sim 8.9 \times 10^{-5}$) and 150 MPa ($\sigma/E \sim 7.6 \times 10^{-4}$). The creep rate has been normalized by the absolute temperature and the Young's modulus to take into account the temperature dependence of the pre-exponential term in the Mukherjee-Bird-Dorn creep equation [28].

Fig. 9: Stress dependence of the true activation energy for tensile creep showing four deformation regimes (I, II, III and IV). The activation energy for the lattice diffusion of Ni tracers, depicted by the upper horizontal broken line, is based on the data of Frank *et al.* [31].

Fig. 10: Map of the stress-temperature space depicting the conditions under which inverse (I), multiple (M) and normal (N) primary creep curves were observed during tension creep of near-stoichiometric NiAl.

Fig. 11: Stress-temperature space where inverse (I) and normal (N) primary creep curves were observed during creep of near-stoichiometric NiAl showing a shift to higher stresses

and higher temperatures for the compression creep data [15,24,25] compared to the tension creep results.

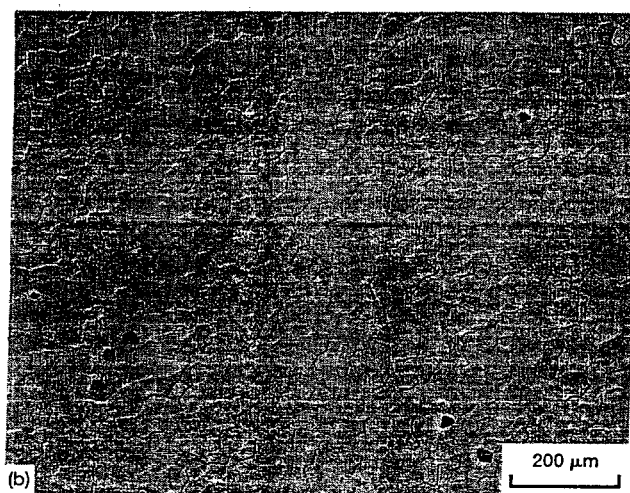
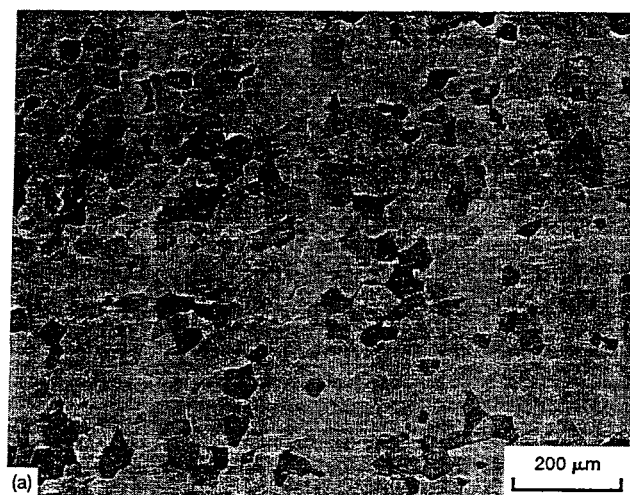
Fig. 12: Comparison of the stress dependence of the true activation energy for creep of near-stoichiometric NiAl determined in compression [13, 24,25] and tension creep experiments. The activation energy for the lattice diffusion of Ni tracers, depicted by the upper horizontal broken line, is based on the data of Frank *et al.* [31].

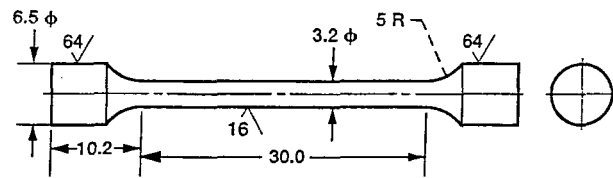
Fig. 13: Comparison of the true creep rate vs. true stress for as-cast and extruded, near-stoichiometric NiAl tested in compression [15,24,25] and tension between 800 and 1200 K. The average grain size for the compression specimens was 35 μm .

Fig. 14(a-i): Schematic showing the expected sequence of atom-vacancy exchanges occurring within the core of a $\langle 100 \rangle \{010\}$ edge dislocation during climb assuming a six-jump cycle. The dislocation core structure is based on atomic simulation studies [58]. The Al and Ni atoms are represented by the solid and open circles, respectively, while the vacancy is represented by the square. The positions of atoms 1 to 3 are indicated in each jump sequence, where the arrow denotes the direction of motion of an Al or a Ni vacancy.

Fig. 15(a-b): Schematic showing the probable sequence of atom-vacancy exchanges occurring within the core of a $\langle 100 \rangle \{010\}$ edge dislocation during climb by one atomic step assuming a next nearest neighbor jump cycle. The dislocation core structure is based on atomic simulation studies [58]. The Al and Ni atoms are represented by the solid and

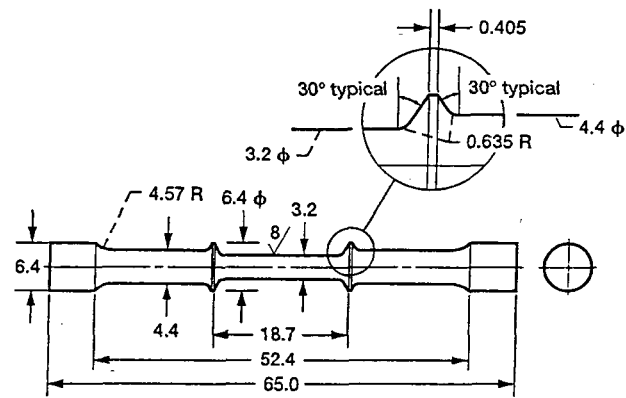
open circles, respectively, while the vacancy is represented by the square. The positions of atoms 1 to 6 and Al and Ni vacancies denoted as A and B, respectively, are indicated in (a) the initial and (b) the final configuration, where the arrow denotes the direction of motion of the Al and Ni atoms.





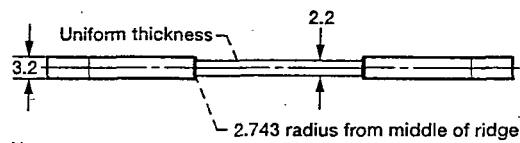
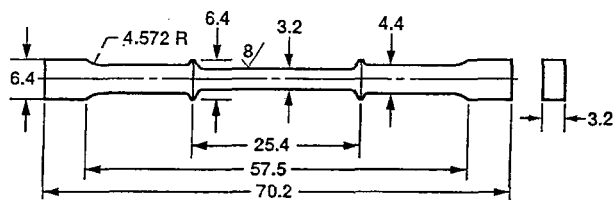
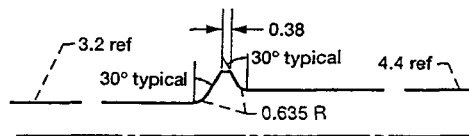
All dimensions in mm

(a)



All dimensions in mm

(b)



Note:

8/ surface finish all over

All dimensions in mm

(c)

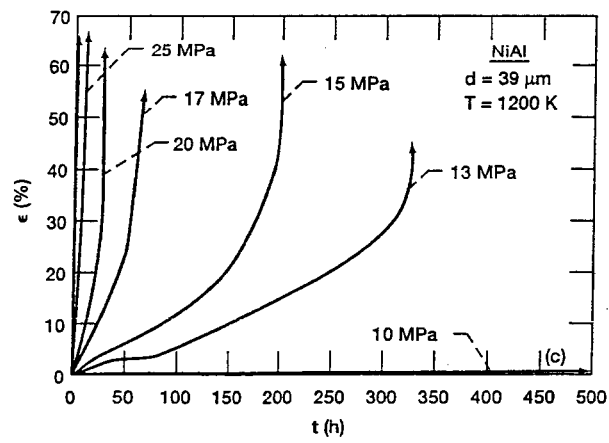
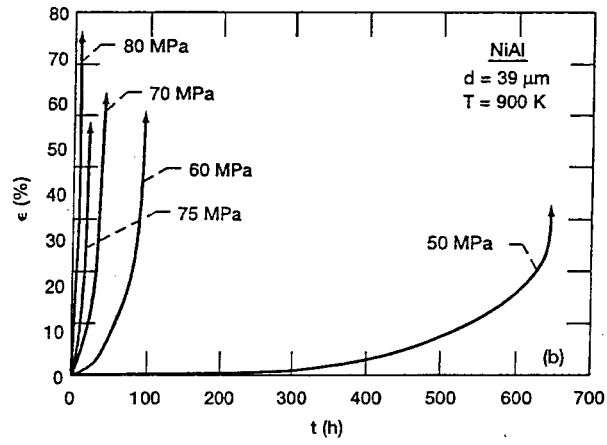
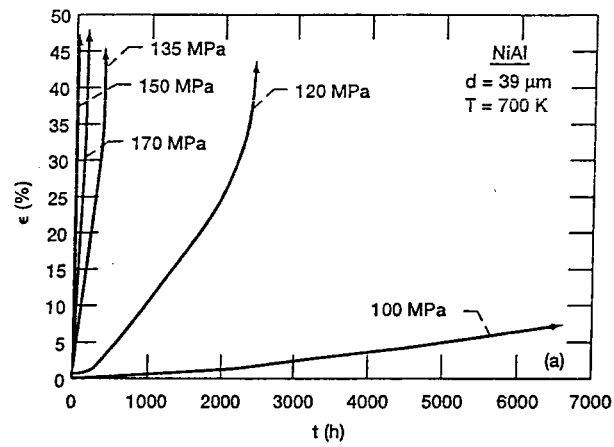


Figure 3

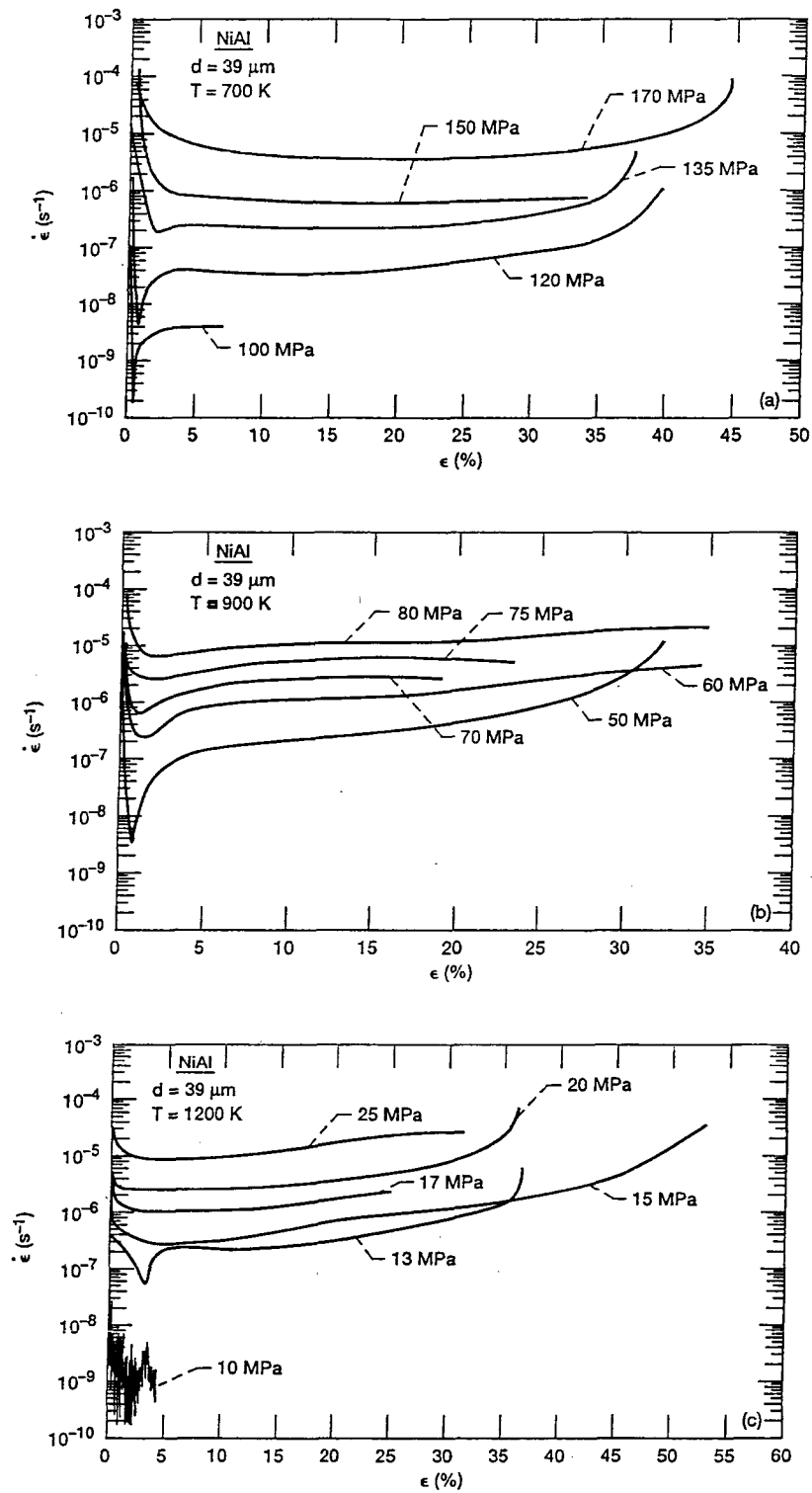
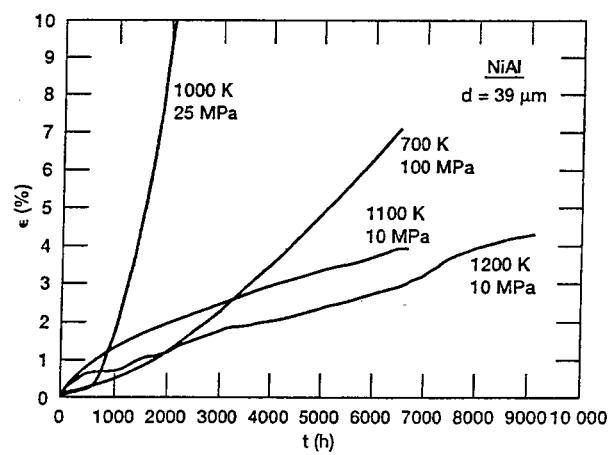


Figure 4



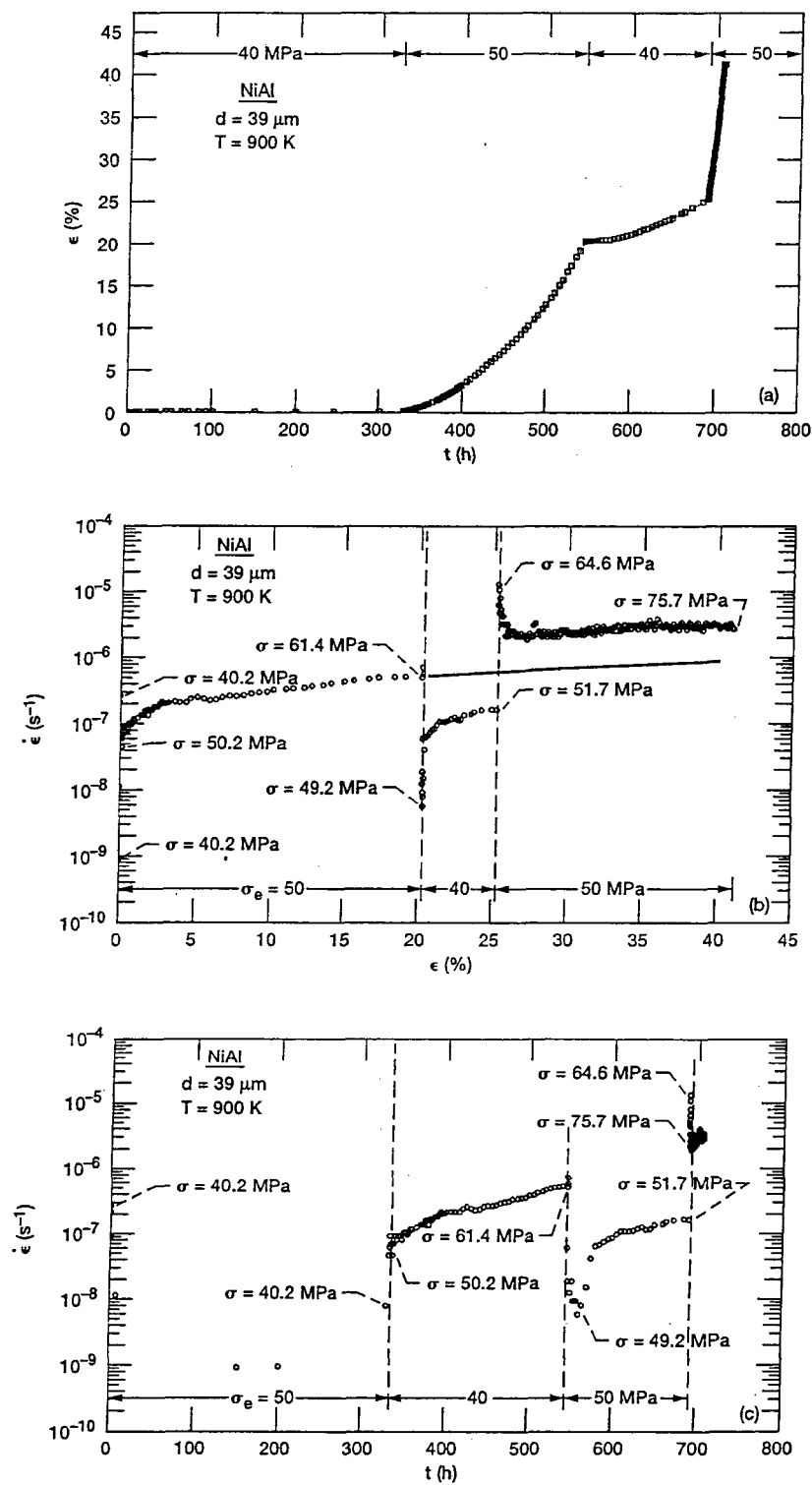


Figure 6

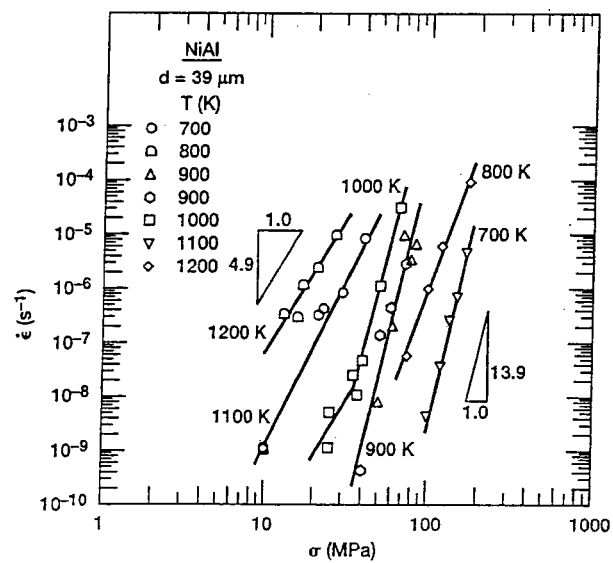


Fig 7.

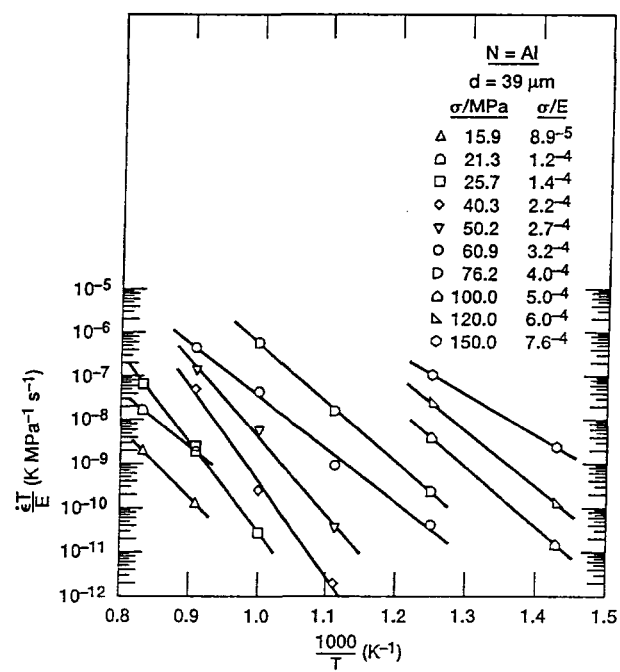


Fig 8.

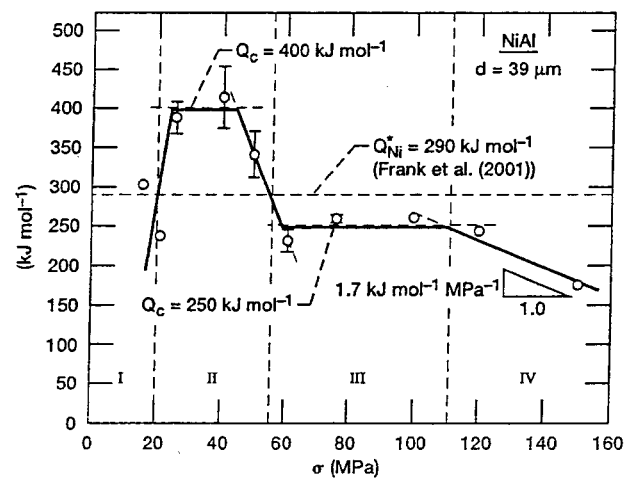


Fig 9.

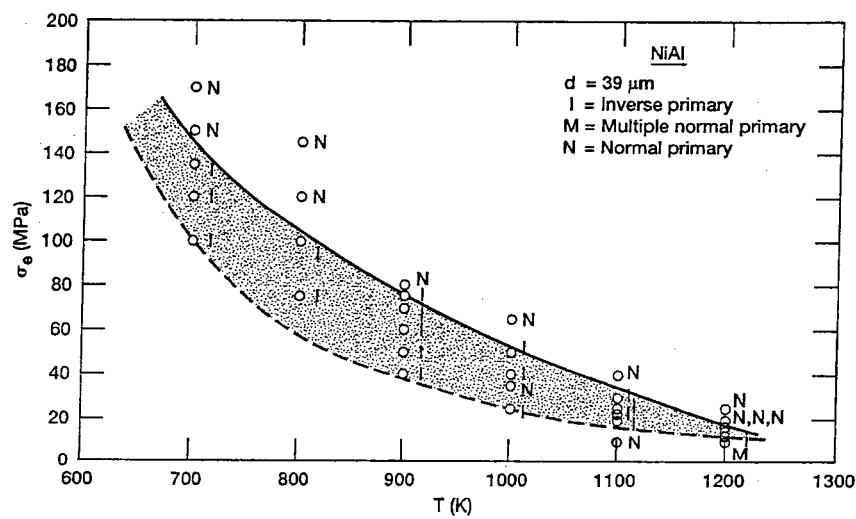


Figure 10

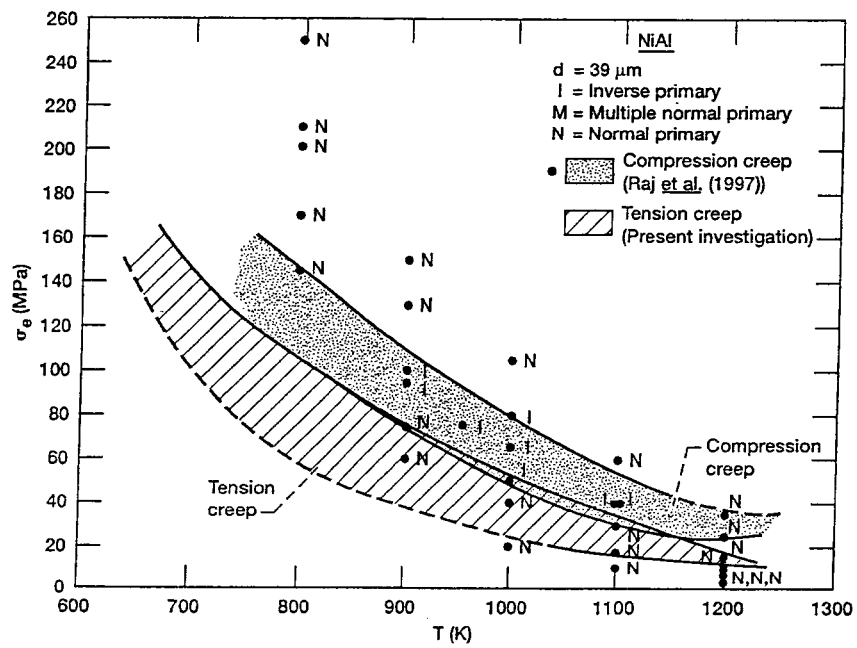
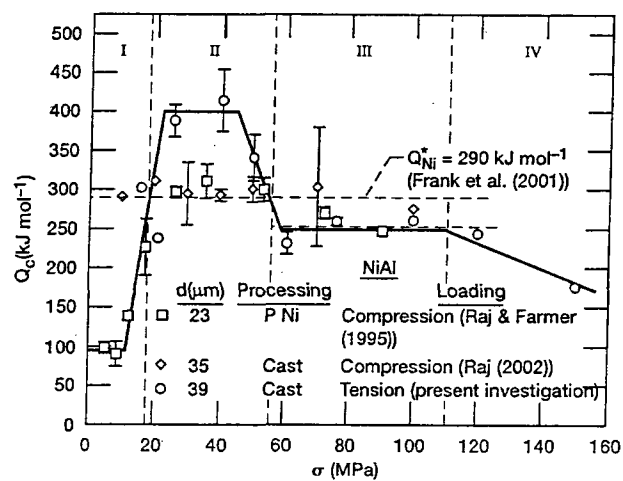


Figure 11



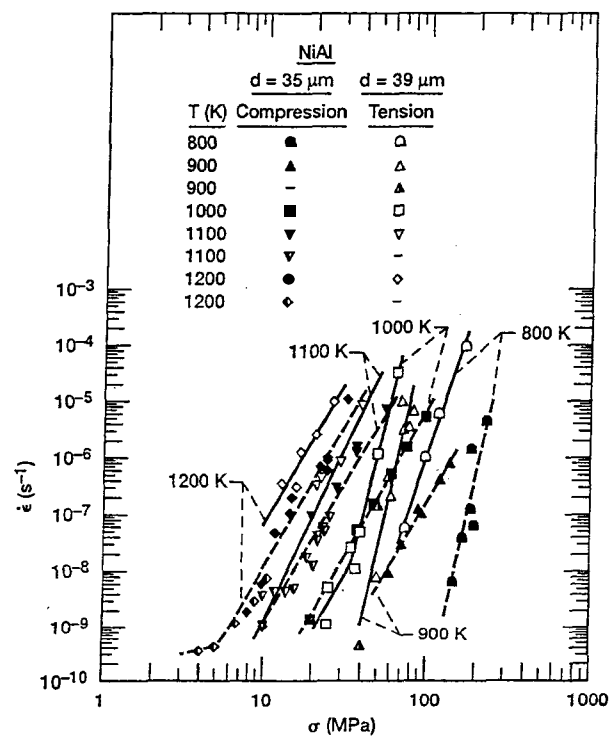


Fig 13.

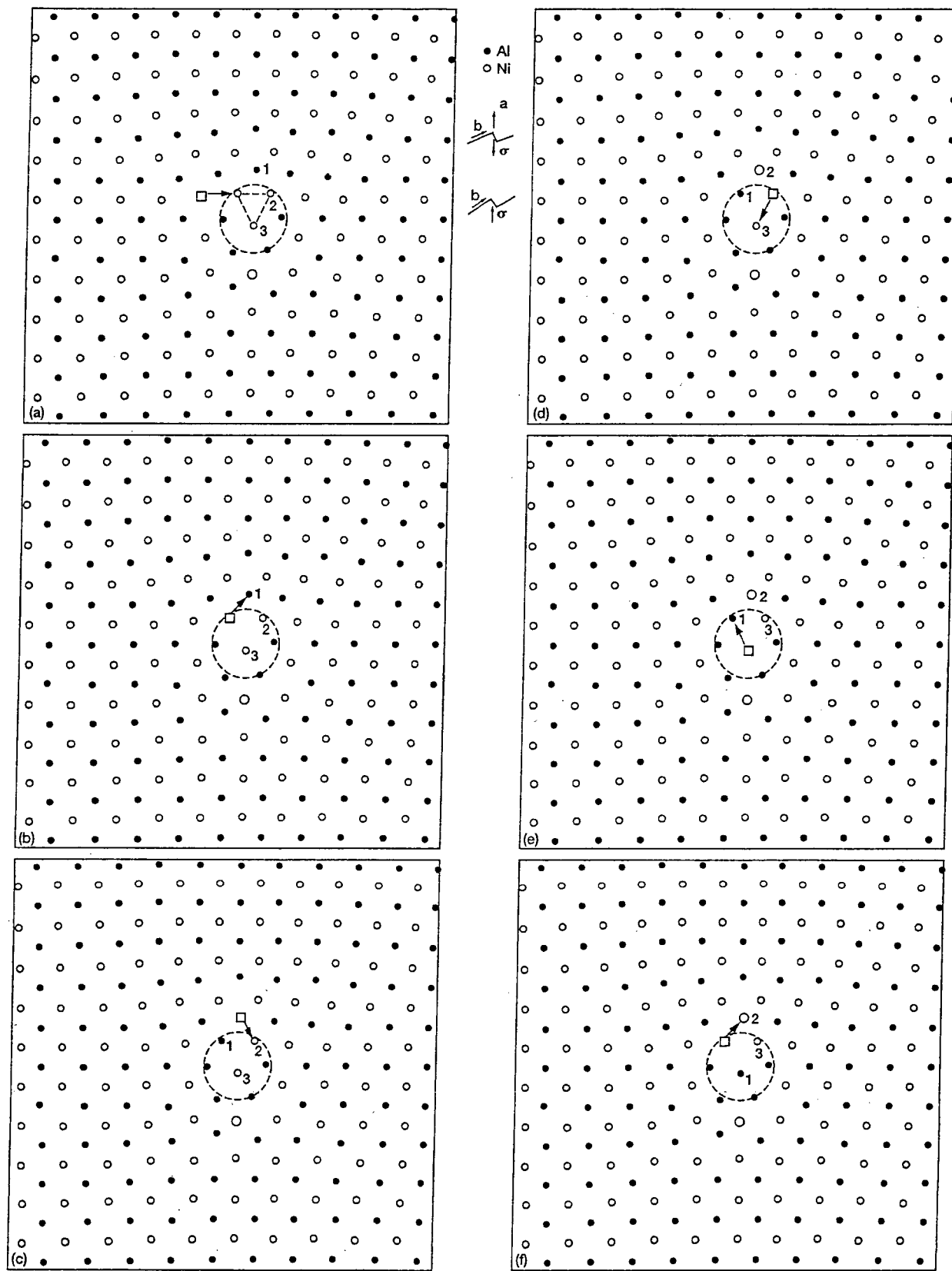


Figure 14

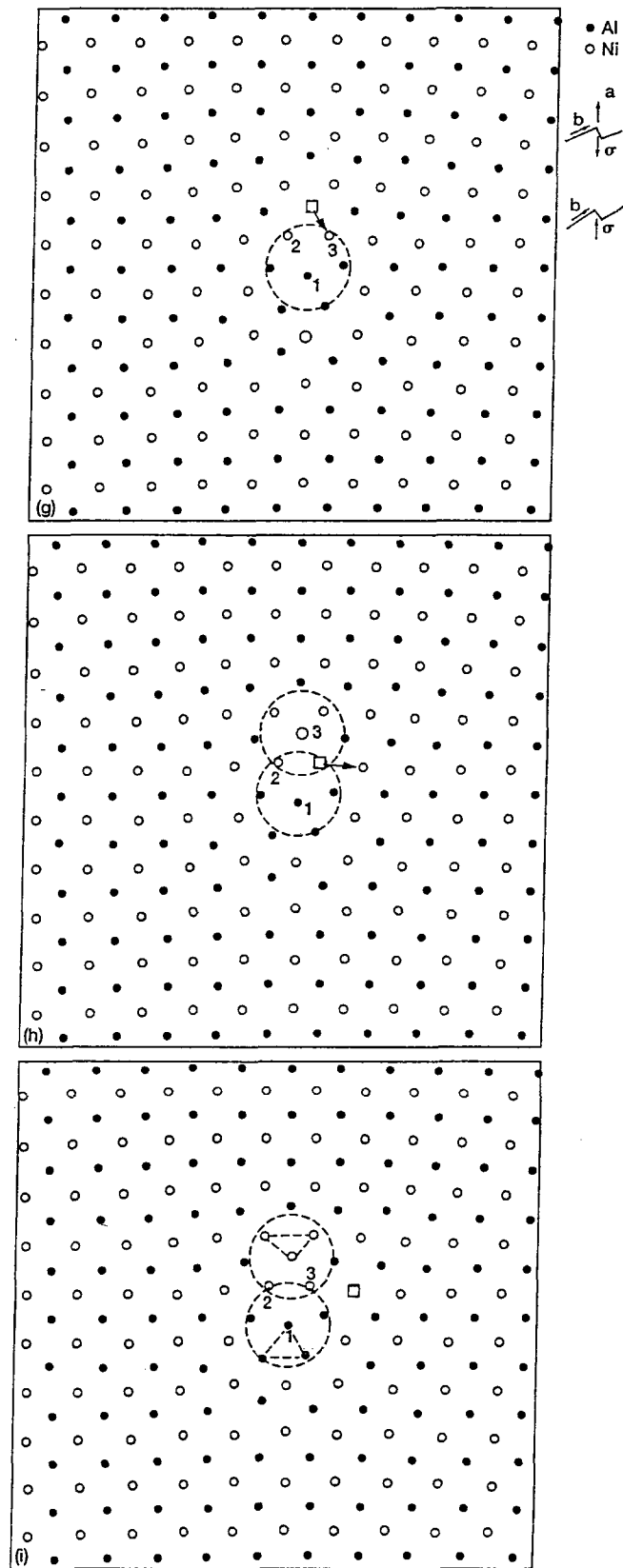


Figure 14 Concluded

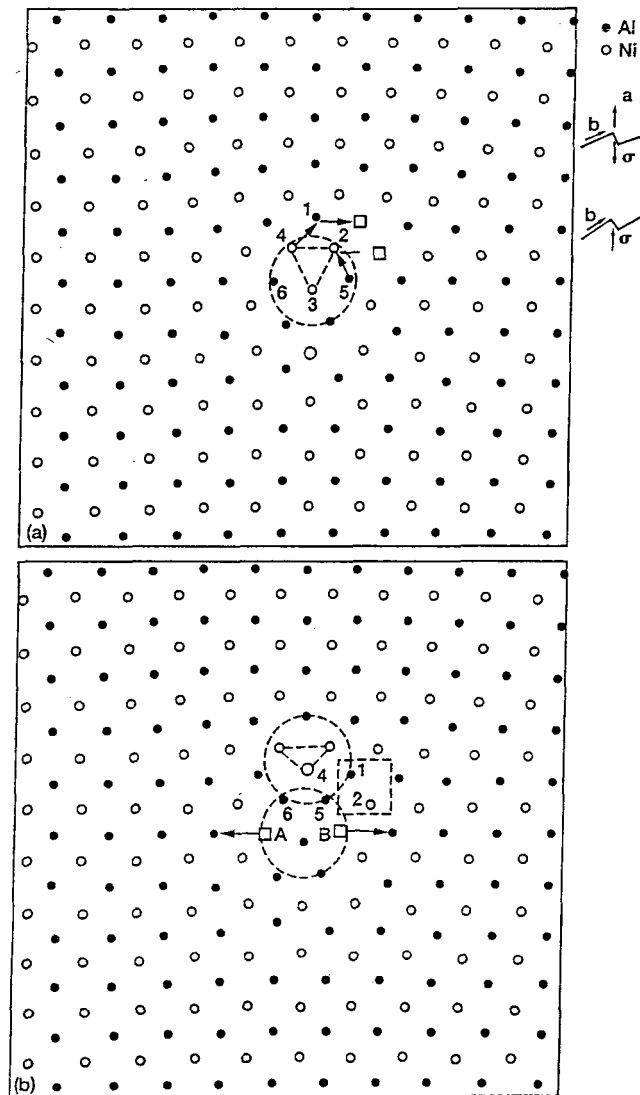


Figure 15